ROYAL SOCIETY
OF CHEMISTRY

PAPER

High-pressure structural phase transitions and metallization in layered HfS$_2$ under different hydrostatic environments up to 42.1 GPa†

Meiling Hong,[ab] Lidong Dai, [ID] *[a] Haiying Hu, [ID] *[a] Xinyu Zhang,[ab] Chuang Li[ab] and Yu He[ab]

A series of structural, vibrational and electrical transport behaviors for HfS$_2$ were systematically investigated by Raman spectroscopy, electrical conductivity, high-resolution transmission electron microscopy (HRTEM) and atomic force microscopy (AFM) in conjunction with first-principles theoretical calculations in the processes of compression and decompression under different hydrostatic environments. High-pressure Raman scattering and electrical conductivity results revealed that HfS$_2$ underwent two structural phase transitions and metallization at 8.0, 15.2 and 20.5 GPa under non-hydrostatic conditions. The first structural transition was characterized by the appearance of the M1 and M2 Raman peaks and the inflection point in the pressure-dependent electrical conductivity. The second structural transition was identified from the disappearance of the E$_g$, M1 and M2 Raman peaks, the emergence of the M3–M6 Raman peaks, and the discontinuities in the pressure coefficient of the A$_{1g}$ mode and electrical conductivity. As the pressure increased to 20.5 GPa, HfS$_2$ underwent a metallization transition, which was attributed to the closure of the bandgap energy obtained from first-principles theoretical calculations. Under hydrostatic conditions, two structural transformations and metallization of HfS$_2$ occurred at relatively high pressures of 8.2, 17.2 and 23.1 GPa due to different deviatoric stress. Upon decompression, the phase transition was revealed to be reversible under different hydrostatic environments, which was verified by the HRTEM and AFM results. Our acquired results of the crystalline and electronic structures of HfS$_2$ facilitate the understanding of the high-pressure characterization of other HfX$_2$ compounds (X = Se and Te) under different hydrostatic environments.

1. Introduction

Hafnium dichalcogenide HfX$_2$ compounds (X = S, Se and Te) are a group of emergent layered transition metal dichalcogenides (TMDs), where the monolayers constituted of S–Hf–S sandwich structures are piled up along the *c*-axis direction *via* weak van der Waals interlayer forces.[1–3] As a prototypical member of the HfX$_2$ family, HfS$_2$ possesses some extraordinary properties, such as higher electron mobility and current density, which makes it a promising candidate material for use in the applications of field effect transistors (FETs), phototransistors, solar cells and photodetectors.[2,4–6] Under ambient conditions, HfS$_2$ exhibits

three different polytypes categorized by the stacking sequences of the layers, the coordination environment of the hafnium atoms and the structural distortions, including 1T (trigonal), 2H (hexagonal) and 3R (rhombohedral) structures. Among them, 1T-HfS$_2$ has been reported to be the most simple and stable polytype.[7–10]

Previous investigations have disclosed that the pressure is a crucial factor in modulating the high-pressure crystalline and electronic structures of hafnium dichalcogenides, thus leading to the occurrences of structural transition and metallization under high pressure.[8,11–15] Despite some available high-pressure phase stability and structural transition studies for HfSe$_2$ and HfTe$_2$, the relevant research on HfS$_2$ has to date been rather rare. Ibáñez *et al.* (2018) reported the high-pressure Raman spectroscopy of HfS$_2$ up to a limited pressure of 12.7 GPa in a mixture of methanol–ethanol–water (volume ratio: 16 : 3 : 1) as the pressure medium.[11] They observed a new Raman peak within the high-frequency region of the A$_{1g}$ peak at 11.3 GPa, which was tentatively attributed to the occurrence of a first-order phase transition for HfS$_2$. Upon further compression to 12.1 GPa, the A$_{1g}$ peak

[a] Key Laboratory of High-temperature and High-pressure Study of the Earth's Interior, Institute of Geochemistry, Chinese Academy of Sciences, Guiyang, Guizhou 550081, China. E-mail: dailidong@vip.gyig.ac.cn, huhaiying@vip.gyig.ac.cn

[b] University of Chinese Academy of Sciences, Beijing 100049, China

† Electronic supplementary information (ESI) available. CCDC 2177305–2177306. For ESI and crystallographic data in CIF or other electronic format see DOI: https://doi.org/10.1039/d2tc01669a

This journal is © The Royal Society of Chemistry 2022

J. Mater. Chem. C, 2022, **10**, 10541–10550 | **10541**

disappeared and the newly appeared Raman peak became dominant with the rise in pressure. More recently, Grzeszczyk *et al.* (2022) investigated the Raman spectroscopy of bulk HfS_2 using a diamond anvil cell up to 27.0 GPa using crystallographic oil as the pressure medium and revealed the occurrence of two structural transitions within the respective pressure ranges of 5.7–9.8 GPa and 12.8–15.2 GPa.[15] They identified the first structural transition of HfS_2 by the significant weakening of the A_{1g} mode in its Raman spectrum, the disappearance of the ω_1 Raman peak and the emergence of a series of Raman peaks (I–VII). When the pressure was higher than 12.8 GPa, the complete vanishing of the A_{1g} mode and the substantial broadening of the Raman peaks indicated the occurrence of the second structural phase transition. Upon decompression from 27.0 GPa to 1.7 GPa, the Raman spectra of HfS_2 were preserved, suggesting the irreversibility of structural transition. Additionally, some available noble gases (*e.g.*, helium, neon, xenon, *etc.*) have been proposed to be better choices for providing hydrostatic conditions under higher pressure since they remain soft even after solidification.[16–19]

However, HfS_2 shares similar crystalline and electronic structures to those of $HfSe_2$ which has been found to undergo metallization under high pressure.[12] Recently, Andrada-Chacón *et al.* (2021) have studied the high-pressure electronic properties of $HfSe_2$ by virtue of *in situ* visible-near infrared absorption measurements using a diamond anvil cell.[12] Their results showed that the transmittance of $HfSe_2$ significantly reduced with increasing pressure and became almost negligible at 10.2 GPa, indicating the occurrence of metallization. Furthermore, the pressure-induced metallization of $HfSe_2$ was corroborated by first-principles theoretical calculations results as being due to the overlap of valence and conduction bands. Until now, there have been no available related reports as to whether HfS_2 undergoes metallization under high pressure.

In this study, we comprehensively explored the structural, vibrational and electrical transport properties of HfS_2 up to 42.1 GPa by means of Raman spectroscopy, electrical conductivity, high-resolution transmission electron microscopy and atomic force microscopy measurements in combination with first-principles theoretical calculations in the processes of compression and decompression under different hydrostatic environments. Furthermore, we discuss in detail two structural phase transitions and the metallization of HfS_2 under different hydrostatic environments.

2. Experimental

2.1 Sample preparation and characterization

Commercially available HfS_2 with its high purity of 99.999% was purchased from Leshang Kaiyada Company, Sichuan, China. The starting sample was synthesized *via* chemical vapor deposition, which has been extensively employed to prepare high-quality hafnium dichalcogenides.[5,6,20] X-Ray diffractometry (XRD) of the initial sample was conducted using a Panalytical Empyrean diffractometer over a diffraction angle (2θ) range from 10° to 70° using copper Kα1 radiation ($\lambda = 1.5406$ Å).
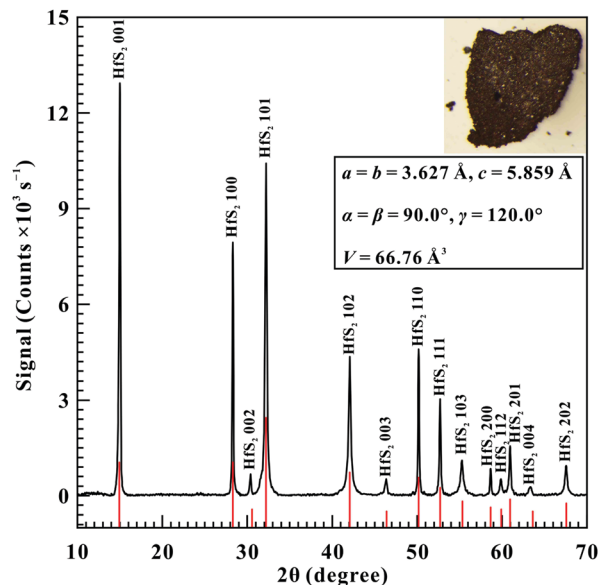

Fig. 1 Typical XRD pattern of the starting sample. Herein, the black solid line represents our measured XRD results and the red vertical lines are the standardized diffraction peak positions of trigonal structured HfS_2. All of these collected diffraction peaks are labelled with Miller indices. Inset: Optical microscope photograph and the corresponding lattice parameters of the starting HfS_2 sample.

Our acquired XRD data were processed using the MDI Jade 6.5 software. As shown in Fig. 1, our collected XRD pattern matches well with the standardized diffraction peaks from JCPDS card No. 28-0444. Therefore, the starting sample can be well identified as a trigonal structure in the space group $P\bar{3}m1$. Additionally, some representative lattice parameters of the starting sample were determined as follows: $a = b = 3.627$ Å, $c = 5.859$ Å, $\alpha = \beta = 90.0°$, $\gamma = 120.0°$ and $V = 66.76$ Å^3. Furthermore, the relationship between the diffraction angle (2θ) and the full width at half maximum (FWHM) for HfS_2 is shown in Table S1 (ESI†). The results revealed that the starting sample possessed high crystallinity quality, with a crystallinity of 97.76%.

2.2 High-pressure Raman spectroscopy measurements for HfS_2

In situ high-pressure Raman spectroscopy and electrical conductivity experiments of HfS_2 were conducted in a symmetric-type diamond anvil cell equipped with a pair of diamonds with a culet diameter of 200 μm and bevel angle of 10°. We precompressed a piece of 250 μm thick T-301 stainless steel gasket into approximately 50 μm. Afterwards, a central hole of 100 μm in diameter was drilled as the sample chamber using a laser drilling machine. HfS_2 together with several ruby balls for pressure calibration were loaded into the sample chamber. Two sets of independent high-pressure Raman scattering experiments were performed for HfS_2, one without pressure medium to achieve non-hydrostatic conditions and another one using helium as the pressure medium to afford hydrostatic conditions, respectively. Helium exhibits stable physicochemical properties and high hydrostaticity, and thus has been widely applied in previous high-pressure investigations.[16–19,21,22]

The uncertainties of pressure calibration were less than 5% and 3% under non-hydrostatic and hydrostatic conditions, respectively. The Raman spectra of HfS_2 were measured using a Renishaw 2000 Micro-Confocal Raman spectrometer (TCS SP8, Leica, Renishaw) equipped with an Olympus charge coupled device (CCD) camera. The Raman spectra of HfS_2 were collected at a wavelength of 514.5 nm in Argon ion excitation source backscattering configuration. Prior to each of the Raman scattering experiments, the wavenumber of Raman spectrometer was calibrated using single-crystalline silicon as a standard material. To protect the sample from destruction, we set the incident beam intensity and exposure time to 1 mW and 60 s, respectively. All of the Raman spectra for HfS_2 were fitted using a Lorentzian-type function to extract their corresponding Raman peak positions at each experimental pressure point.

2.3 High-pressure electrical conductivity measurements for HfS_2

A clean T-301 stainless steel gasket was pre-pressurized in order to form a circular dent at a pressure of ~ 10.0 GPa. Subsequently, a 180 μm of concentric hole was drilled across the circular stainless steel dent using a laser drilling machine. To guarantee electrical isolation between the electrodes and gasket, insulation powder consisting of boron nitride and epoxy completely covered and was tightly compacted into the hole at ~ 15.0 GPa. Then, another new central hole with a diameter of 100 μm was drilled as the sample chamber. Furthermore, the remaining portion of the gasket was completely coated by insulating cement. Two pieces of hand-cut platinum foils with a thickness of 10 μm were then adhered to the upper and lower counterparts of the sample using silver epoxy. No pressure medium was employed to assure good contact between the electrodes and sample, and minimize experimental error. The complex impedance spectra of HfS_2 were measured by the connection interface of a Solartron-1260 impedance/gain phase analyser and Solartron-1296 dielectric interface within a frequency range of 10^{-1}–10^7 Hz. Two representative signal voltages of 1.0 V and 30 mV were applied before and after the occurrence of metallization, respectively. Variable-temperature electrical conductivity experiments were conducted using the refrigeration effect of liquid nitrogen, and the temperature was precisely monitored by a K-type thermocouple stuck to the side of a diamond anvil. The uncertainty of the temperature calibration was not more than ~ 5 K. More detailed sample assembly and experimental procedures for the measurement of electrical conductivity have been described in our previous investigations.[18,19,21,22]

2.4 High-resolution transmission electron microscopy (TEM) and atomic force microscopy (AFM) observations for HfS_2

Microstructural observations of both the starting and recovered samples under different hydrostatic conditions were conducted by high-resolution TEM and AFM. A Tecnai G2 F20 S-TWIN TMP transmission electron microscope was operated at an accelerating voltage of 200 kV. A small chip of the sample was homogenously dispersed in ethanol in an ultrasonic cleaner. Subsequently, a droplet of liquid was transferred onto a carbon-film-coated copper grid for HRTEM observations. Digital Micrograph software was employed to accurately determine the interplanar spacings of the starting and recovered samples. To determine the sample composition, TEM equipped with an energy dispersive X-ray spectroscopy (TEM-EDS) probe was carried out. As seen in Fig. S1 (ESI†), besides the signals of the carbon-film-coated copper grid (the signals of carbon and copper), the TEM-EDS spectrum displays characteristic signals of both hafnium and sulphur, suggesting the high purity of the starting HfS_2 sample.

AFM is a non-destructive method of characterizing the three-dimensional (3D) surface topography of starting and recovered samples at the nanoscale. Small amounts of the starting and recovered samples were uniformly distributed on clean glass substrates for AFM observation, which was performed using a Multimode 8 mass spectrometer with a high imaging pixel of 512×512. In order to avoid contact between the cantilever probe tip and sample surface, tapping mode was selected to image the surface topography of the samples.

2.5 First-principles theoretical calculations for HfS_2

First-principles theoretical calculations were carried out for HfS_2 by means of Kohn-Sham density functional theory (DFT) and pseudopotential methods in the Material Studio package with the standard Cambridge Sequential Total Energy Package (CASTEP) code.[23] The generalized gradient approximation (GGA) along with the Perdew–Burke–Ernzerhof (PBE) functions were chosen to describe the geometric optimization and band structure calculations, respectively. The structural optimizations of HfS_2 were implemented through the Brogden–Fletcher–Goldfarb–Shanno (BFGS) minimization algorithm within the CASTEP code. In order to determine the high-pressure crystalline structure, we carried out the structural research of HfS_2 within the pressure range of 0–40.0 GPa at the Hefei advanced computing center. Furthermore, a new high-pressure phase of $I4/mmm$ was predicted. For the $P\bar{3}m1$ phase, we selected a Monkhorst–Pack K point mesh of $5 \times 5 \times 5$ and cutoff energy of 500 eV, respectively. As for the $I4/mmm$ phase, a relatively high kinetic cutoff energy of 800 eV and Monkhorst–Pack K point mesh of $9 \times 9 \times 5$ were applied to realize a high convergence. More details of the first-principles theoretical calculations have been published previously.[18,24,25]

3. Results and discussion

3.1 High-pressure Raman spectra results of HfS_2

Raman spectroscopy has been proved to be a powerful method of characterizing the crystalline structure of hafnium dichalcogenides under high pressure.[11,12,15] As depicted in Fig. 2a, at a fixed pressure of 1.2 GPa, we observed a weak Raman peak at 261.1 cm^{-1} and another sharp Raman peak at 338.4 cm^{-1} within the wavenumber range of 100–450 cm^{-1} under non-hydrostatic conditions, which can be assigned as the in-plane (E_g) and out-of-plane (A_{1g}) vibrational modes of the S–Hf–S crystalline lattice, respectively. Furthermore, these detected Raman peaks are in accordance with previous results.[3,5,6,11,15,26]
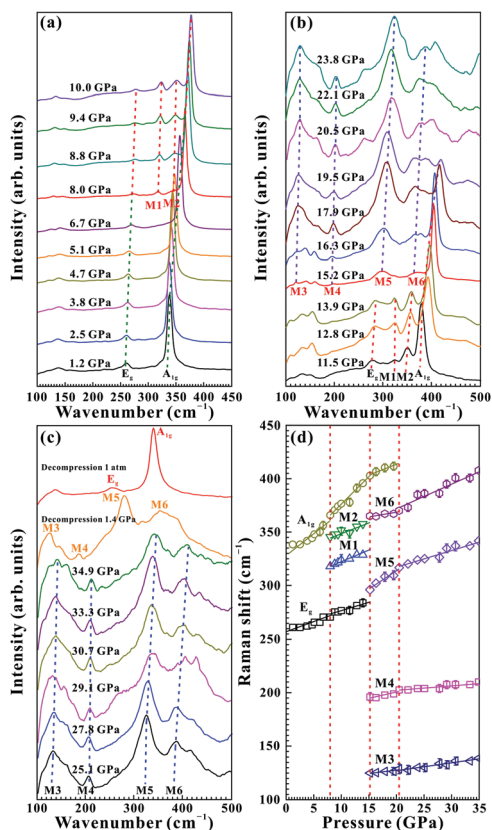
This journal is © The Royal Society of Chemistry 2022

J. Mater. Chem. C, 2022, **10**, 10541–10550 | **10543**

Fig. 2 (a–c) High-pressure Raman spectra for HfS$_2$ within the pressure range of 1.2–34.9 GPa during compression and the selected Raman spectra at two representative pressures of 1.4 GPa and 1 atm during decompression. (d) Pressure dependence of the Raman shifts for HfS$_2$ under non-hydrostatic conditions. The errors in the Raman wavenumbers are within the size of the symbols.

Fig. 2a–c show the high-pressure Raman spectra of HfS$_2$ within the pressure range of 1.2–34.9 GPa under non-hydrostatic conditions. The pressure-dependent Raman shift relations (the pressure coefficient, dω/dP, where ω is the Raman shift and P is the pressure) and the corresponding fitting results for HfS$_2$ in the processes of compression and decompression under different hydrostatic environments are displayed in Fig. 2d and Table 1 in detail. It can be seen that both the E$_g$ and A$_{1g}$ Raman modes of HfS$_2$ shifted towards higher wavenumbers with increasing pressure at the respective rates of 1.63 cm^{-1} GPa^{-1} and 3.99 cm^{-1} GPa^{-1}. Noticeably, the magnitude in the pressure coefficient of A$_{1g}$ mode for HfS$_2$ is approximately twice that of the E$_g$ mode, suggesting that pressure has a more significant influence on the out-of-plane vibration than the in-plane vibration. As a matter of fact, our observed anisotropic compressibility in the sample has also been detected in other TMDs.[11,12,15,27–29] As the pressure was enhanced up to 8.0 GPa, two new Raman peaks at the respective wavenumbers of 317.9 cm^{-1} and 345.6 cm^{-1} emerged, which is typically characteristic of the occurrence of structural transition. Here, we denoted the Raman peaks at 317.9 cm^{-1} and 345.6 cm^{-1} as the M1 and M2 modes, respectively. Above 8.0 GPa, both the M1 and M2 Raman peaks displayed blue

shifts, and became gradually more intense with the rise in pressure. When the pressure was continuously increased to 15.2 GPa, the three characteristic Raman peaks of E$_g$, M1 and M2 vanished. At the same time, four new Raman peaks at the correspondent wavenumber positions of 125.3, 195.3, 296.2 and 365.9 cm^{-1} (denoted as M3, M4, M5 and M6 modes, respectively) appeared. Further, the A$_{1g}$ mode exhibited an obvious discontinuity in Raman shift at 15.2 GPa, since the pressure coefficient of A$_{1g}$ mode was converted from a steep value of 4.84 cm^{-1} GPa^{-1} at 8.0–15.2 GPa to a gentle value of 2.04 cm^{-1} GPa^{-1} at 15.2–20.5 GPa. In brief, three remarkable high-pressure behaviours, including the disappearance of E$_g$, M1 and M2 Raman peaks, the emergence of M3–M6 Raman peaks and the discontinuity in the pressure coefficient of A$_{1g}$ mode, provided robust evidence for the occurrence of structural transition. In addition, we observed that the A$_{1g}$ mode of the sample tended to weaken as the pressure was increased from 15.2 GPa to 19.5 GPa. When the pressure was higher than 20.5 GPa, the A$_{1g}$ mode completely disappeared, accompanied by discontinuities in the pressure coefficients of the M3–M6 Raman modes. At 15.2–20.5 GPa, the M3 and M6 Raman modes exhibited gentler slopes of 0.64 cm^{-1} GPa^{-1} and 0.90 cm^{-1} GPa^{-1} and two steeper rates of 1.21 cm^{-1} GPa^{-1} and 3.44 cm^{-1} GPa^{-1} were observed for the M4 and M5 modes, respectively. Beyond 20.5 GPa, the M3 and M6 Raman modes showed steeper rates of 0.74 cm^{-1} GPa^{-1} and 2.47 cm^{-1} GPa^{-1}, and two gentler rates of 0.50 cm^{-1} GPa^{-1} and 1.70 cm^{-1} GPa^{-1} were observed for the M4 and M5 modes, respectively. Therefore, the disappearance of the A$_{1g}$ mode and the discontinuities in the pressure coefficients of the M3–M6 Raman modes suggest that HfS$_2$ underwent a structural transition at 20.5 GPa. Upon further compression above 20.5 GPa, the Raman peaks of the sample showed pronounced broadening and weakening with the rise in pressure. In summary, our high-pressure Raman spectra results revealed that HfS$_2$ underwent three structural transitions at 8.0, 15.2 and 20.5 GPa under non-hydrostatic conditions.

Upon decompression, four characteristic Raman peaks of M3–M6 were preserved as the pressure decreased to 1.4 GPa. Upon further decompression to 1 atm, two predominant Raman peaks at 253.8 cm^{-1} and 338.4 cm^{-1} reappeared, which implies the reversibility of structural phase transition. Nevertheless, there exists a large pressure hysteresis effect for HfS$_2$ during decompression, which is possibly caused by the sluggish kinetics at room temperature.

However, our acquired high-pressure Raman spectra of HfS$_2$ under hydrostatic conditions are analogous to those collected under non-hydrostatic conditions, as illustrated in Fig. S2 (ESI†). Some similar phenomena, including the emergence of the M1 and M2 Raman peaks at 8.2 GPa, the disappearance of the E$_g$, M1 and M2 Raman peaks accompanied by the appearance of the M3–M6 Raman peaks and the discontinuity in the pressure coefficient of the A$_{1g}$ mode at 17.2 GPa, followed by the complete disappearance of the A$_{1g}$ mode and the inflection points in the pressure coefficients of the M3–M6 modes at 23.1 GPa, were observed under hydrostatic conditions. Meanwhile, the reversibility of structural transition under hydrostatic conditions was

Table 1 Pressure-dependent Raman wavenumbers ($d\omega/dP$, cm^{-1} GPa^{-1}) for HfS$_2$ in the processes of compression and decompression under non-hydrostatic and hydrostatic conditions. Here, ω (cm^{-1}) and P (GPa) represent the Raman wavenumber and pressure, respectively

Pressure conditions		Pressure (GPa)	ω (cm^{-1})	$d\omega/dP$ (cm^{-1} GPa^{-1})	ω (cm^{-1})	$d\omega/dP$ (cm^{-1} GPa^{-1})
Non-hydrostatic	Compression	1.2–8.0	261.1 (E$_g$)	1.63	338.4 (A$_{1g}$)	3.99
		8.0–15.2	270.8 (E$_g$)	1.89	365.9 (A$_{1g}$)	4.84
			317.9 (M1)	1.85	345.6 (M2)	1.85
		15.2–20.5	—	—	402.9 (A$_{1g}$)	2.04
			125.0 (M3)	0.64	195.9 (M4)	1.21
			296.2 (M5)	3.44	365.1 (M6)	0.90
		20.5–34.9	128.9 (M3)	0.74	202.6 (M4)	0.50
			316.7 (M5)	1.70	370.0 (M6)	2.47
	Decompression	34.9–1.4	138.8 (M3)	0.57	209.9 (M4)	0.48
			341.9 (M5)	1.52	407.7 (M6)	1.51
		1 atm	253.8 (E$_g$)	—	338.4 (A$_{1g}$)	—
Hydrostatic	Compression	0.7–8.2	261.1 (E$_g$)	1.38	339.6 (A$_{1g}$)	3.28
		8.2–17.2	270.8 (E$_g$)	1.94	363.6 (A$_{1g}$)	4.29
			316.7 (M1)	1.45	338.4 (M2)	2.72
		17.2–23.1	—	—	406.6 (A$_{1g}$)	2.87
			121.6 (M3)	1.10	196.5 (M4)	0.91
			298.6 (M5)	4.13	365.9 (M6)	1.20
		23.1–36.1	127.7 (M3)	0.70	200.1 (M4)	1.14
			322.7 (M5)	2.11	373.1 (M6)	2.84
	Decompression	36.1–1.6	137.6 (M3)	0.42	211.2 (M4)	0.46
			353.9 (M5)	1.53	420.8 (M6)	1.18
		1 atm	253.8 (E$_g$)	—	338.5 (A$_{1g}$)	—

revealed by the recoverable Raman spectrum of the sample decompressed to 1 atm. The discrepancy in the phase transition pressures of HfS$_2$ under different hydrostatic environments was possibly related to the deviatoric stress within the sample chamber. As shown in Fig. S3 (ESI†), the deviatoric stress within the sample chamber was found to be low below 10.0 GPa (<1.0 GPa), which provides a reasonable explanation for the similar structural transition pressures at ~8.0 GPa under different hydrostatic environments. When the pressure was continuously enhanced above 10.0 GPa, the deviatoric stress within the sample chamber increased progressively, which played a vital role in facilitating the occurrences of the structural transformations beyond 10.0 GPa under non-hydrostatic conditions, as previously reported in other TMDs (e.g., MoS$_2$, ReS$_2$, WSe$_2$, etc).[29–31] Furthermore, in a comprehensive comparison of the structural transition pressure and bulk moduli for some representative TMDs, we found that the structural transition pressures enhanced from 8.0, 11.3, 14.0, 19.0 to 41.0 GPa with increasing bulk modulus from 19, 23, 39, 57 to 72 GPa for HfS$_2$, ReS$_2$, MoTe$_2$, MoS$_2$ and WSe$_2$, which is in good agreement with previous investigations.[11,12,28,29,32,33]

Both the previous high-pressure Raman scattering investigations of Grzeszczyk et al. (2022) and ours measured the Raman spectroscopy of HfS$_2$ in the processes of compression and decompression, and found that HfS$_2$ underwent two structural phase transitions at similar pressure ranges (5.7–9.8 GPa and 12.8–15.2 GPa from the study by Grzeszczyk et al. (2022)).[15] However, there exist some obvious discrepancies, including the identification of pressure-induced structural transitions and the reversibility of high-pressure structural phase transition for HfS$_2$. All of these discrepancies are possibly related to (i) the difference in the hydrostatic environment, the use of crystallographic oil as the pressure medium by Grzeszczyk et al. (2022), and the use of helium as the pressure medium in our present study (helium as a pressure medium can provide good

hydrostatic conditions, which has been widely applied to explore the physicochemical properties of many materials at high pressure in diamond anvil cells);[16–19,21,22] (ii) the difference in the degree of decompression (previous Raman scattering measurements were conducted on HfS$_2$ decompressed from 27.0 to 1.7 GPa at a pressure interval of ~3.5 GPa, and we conducted Raman spectroscopy experiments of a sample decompressed from 36.1 GPa to 1 atm at a pressure interval of ~1.2 GPa).

3.2 High-pressure electrical conductivity results of HfS$_2$

As usual, pressure-induced structural transition is accompanied by a substantial modification in the electrical transport properties of TMDs.[28–30] Fig. 3 displays the Nyquist plots of the complex impedance spectra for HfS$_2$ under 1.8–39.6 GPa and atmospheric temperature conditions. Below 7.7 GPa, the impedance spectra of the sample feature a semicircular arc and an additional tail within their corresponding high frequency and low frequency ranges, which stand for the grain interior and grain boundary conduction mechanisms, respectively. Within the pressure range of 7.7–17.8 GPa, it is clear that only one semicircular arc from the conduction mechanism of grain interior was observed. When the pressure exceeded 19.8 GPa, the impedance spectra of the sample emerged in the fourth quadrant. In order to quantify the electrical resistances of HfS$_2$, all of these measured Nyquist plots were fitted using the equivalent circuit in the ZView software package. From 1.8 GPa to 5.7 GPa, the equivalent circuit composed of the series connection of R_{gi}–CPE$_{gi}$ and R_{gb}–CPE$_{gb}$ (where R_{gi} and R_{gb} are the resistances of the grain interior and grain boundary, respectively; CPE$_{gi}$ and CPE$_{gb}$ are the constant phase elements of the grain interior and grain boundary, respectively) was employed to fit the impedance spectra of the sample. Furthermore, single R_{gi}/CPE$_{gi}$ was established to fit the impedance spectra of HfS$_2$ within the pressure range of

This journal is © The Royal Society of Chemistry 2022

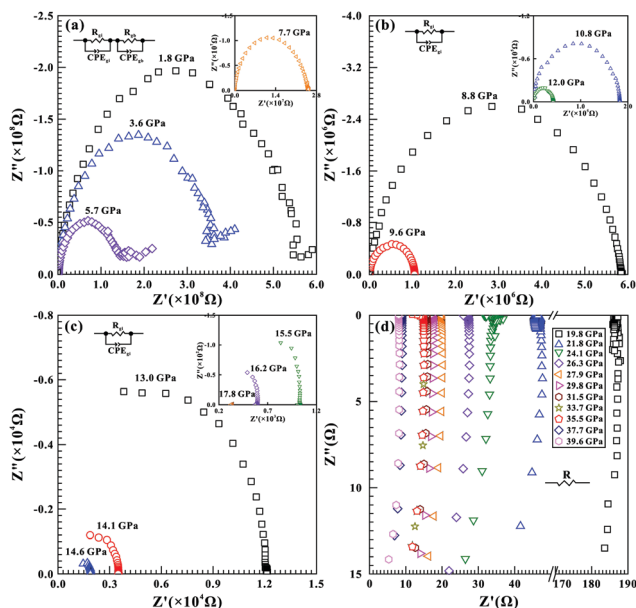J. Mater. Chem. C, 2022, **10**, 10541–10550 | **10545**

Fig. 3 Nyquist plots of the complex impedance spectra for HfS_2 under 1.8–39.6 GPa and atmospheric temperature conditions. Herein, (a) 1.8–7.7; (b) 8.8–12.0; (c) 13.0–17.8 and (d) 19.8–39.6 GPa, respectively. Within the pressure range of 1.8–5.7 GPa, the equivalent circuit made up of the series connection of R_{gi}–CPE_{gi} and R_{gb}–CPE_{gb} (R_{gi} and R_{gb} are the resistances of the grain interior and grain boundary, respectively; CPE_{gi} and CPE_{gb} are the constant phase elements of the grain interior and grain boundary, respectively) was employed to fit the impedance spectra of sample. At 7.7–17.8 GPa, single R_{gi}/CPE_{gi} was established to fit the impedance spectra of HfS_2. When the pressure was higher than 19.8 GPa, a simple resistance (R) was applied to fit the impedance spectra in the fourth quadrant. Here, the symbols of Z' and Z'' stand for the real and imaginary parts of the complex impedance, respectively.

7.7–17.8 GPa. When the pressure was higher than 19.8 GPa, a simple resistance (R) was utilized to determine the electrical conductivity of the sample. The electrical conductivity (σ) of HfS_2 was calculated using the following equation:

$$\sigma = L/SR \tag{1}$$

where L stands for the distance between the electrodes (cm), S represents the cross-sectional area of the electrode (cm^2) and R is the electrical resistance (Ω).

The logarithmic electrical conductivity of HfS_2 against pressure during both processes of compression and decompression is plotted in Fig. 4. Upon compression, the electrical conductivity of HfS_2 monotonously increased with the rise in pressure, whereas four pressure regions of 1.8–7.7, 7.7–16.2, 16.2–21.8 and 21.8–39.6 GPa were obtained from the slope of electrical conductivity *versus* pressure ($d\sigma/dP$, where σ is the electrical conductivity and P is the pressure). At 1.8–7.7 GPa, HfS_2 exhibited a moderate $d\sigma/dP$ value of 0.222 S cm^{-1} GPa^{-1}. Within the pressure range of 7.7–16.2 GPa, the electrical conductivity of the sample was enhanced sharply by approximately four orders of magnitude at a rate of 0.531 S cm^{-1} GPa^{-1}. Nevertheless, a gentle slope of 0.139 S cm^{-1} GPa^{-1} was acquired for HfS_2 at 16.2–21.8 GPa. When the pressure exceeded 21.8 GPa, the electrical conductivity of the sample increased slightly, with a minor $d\sigma/dP$ value of
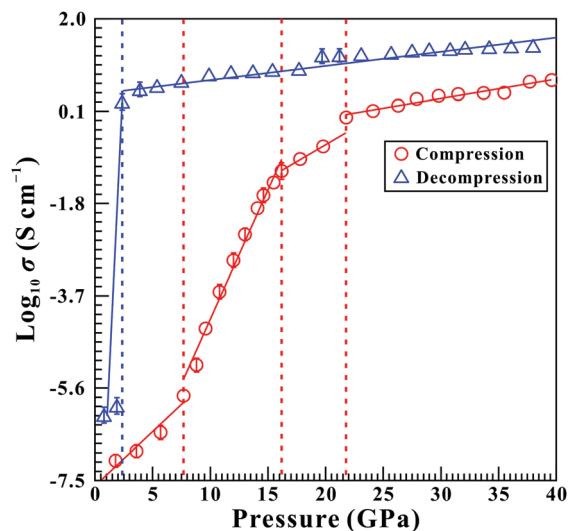

Fig. 4 Logarithmic electrical conductivity of HfS_2 as a function of pressure during both processes of compression and decompression. Here, the solid and dashed lines serve as visual guidance. Errors in electrical conductivities are within the sizes of the symbols.

0.0401 S cm^{-1} GPa^{-1}. And thus, there exist three notable discontinuities in electrical conductivity of HfS_2 at three fixed pressure points of 7.7, 16.2 and 21.8 GPa, which coincides well with our above-mentioned pressure-induced structural transitions of the Raman scattering results under non-hydrostatic conditions. In fact, our previous electrical conductivity investigations on TMDs have already disclosed that a high electrical conductivity value and a feeble pressure dependence of the electrical conductivity relationship are the typical characteristics of metallization.[30,31] In our present study, the electrical conductivity of HfS_2 reached 1 S cm^{-1} at 21.8 GPa. Further, within the pressure range of 21.8–39.6 GPa, a weak pressure-dependent electrical conductivity relationship, with a low $d\sigma/dP$ value of 0.0401 S cm^{-1} GPa^{-1}, was acquired for HfS_2. Therefore, it is reasonable to speculate that the third phase transition of HfS_2 is possibly due to a metallization transition.

During the process of decompression, the electrical conductivity of the sample decreased slightly from 1.39 S cm^{-1} to 0.25 S cm^{-1} as the pressure decreased from 38.0 GPa to 2.4 GPa. Upon further decompression to 1.9 GPa, a remarkable drop in electrical conductivity by almost six orders of magnitude was detected, which is probably related to the reversibility of structural phase transition during decompression.

3.3 Variable-temperature electrical conductivity results of HfS_2

A series of variable-temperature electrical conductivity measurements were implemented to corroborate the occurrence of pressure-induced metallization transition for HfS_2. Fig. 5 represents the logarithmic electrical conductivity of HfS_2 as a function of temperature at six representative pressures of 9.2, 11.0, 14.0, 19.5, 22.7 and 25.1 GPa within the temperature ranges of 123–293 K at an interval of 10 K. As shown in Fig. 5a, HfS_2 displayed a positive temperature-dependent electrical conductivity relationship below 19.5 GPa. When the pressure is higher than
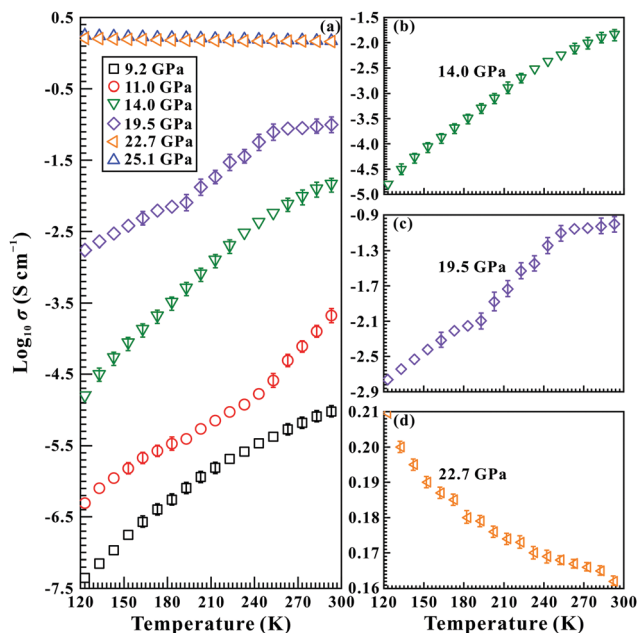
10546 | *J. Mater. Chem. C*, 2022, **10**, 10541–10550

This journal is © The Royal Society of Chemistry 2022

Fig. 5 Variable-temperature electrical conductivity measurements of HfS$_2$ at six characteristic pressures of (a) 9.2, 11.0, 14.0, 19.5, 22.7 and 25.1 GPa. (b and c) The semiconducting properties of HfS$_2$ at two typical pressures of 14.0 GPa and 19.5 GPa. (d) The metallic nature of the sample at a confined pressure of 22.7 GPa. Errors in the electrical conductivities are within the sizes of the symbols.

22.7 GPa, the electrical conductivity of the sample decreased slightly with increasing temperature, as illustrated in Fig. 5d. As is known, semiconductors are characterized by a positive temperature dependence of the electrical conductivity relation-ship, whereas metals show a negative correlation between temperature and electrical conductivity.[18,19,21,22,28–31] And thus, our variable-temperature electrical conductivity results con-firmed the occurrence of a semiconductor-to-metal transition at 22.7 GPa for HfS$_2$. Obviously, the metallization pressure point of HfS$_2$ is considerably higher than that of HfSe$_2$ ($\sim$10.0 GPa),[12] which is possibly related to the stronger electronic coupling effect in HfS$_2$ resulting from the smaller atomic radius and tighter electron orbitals of sulphur compared with those of selenium. Further, a similar phenomenon has also been observed for other TMDs belonging to the transition metal family, such as molybdenum dichalcogenides MoX$_2$ (X = S, Se and Te).[28]

In conclusion, all of these obtained Raman scattering and electrical conductivity results revealed that HfS$_2$ underwent three structural transitions at 8.0, 15.2 and 20.5 GPa under non-hydrostatic conditions. Furthermore, our electrical conductivity results demonstrated that the first and second phase transfor-mations of HfS$_2$ are semiconductor-to-semiconductor transi-tions. As for the third structural transition of HfS$_2$, our variable-temperature electrical conductivity results revealed that it is a metallization transition. It is thus clear that the substantial decrease in the Raman peak intensities of the sample above 20.5 GPa are probably related to the pressure-induced metallic characterization of HfS$_2$.

3.4 HRTEM and AFM results of HfS$_2$

Fig. 6 displays the HRTEM images and their corresponding fast Fourier transform (FFT) patterns of the starting and recovered samples under different hydrostatic conditions. As depicted in Fig. 6a, the initial sample shows clear lattice fringes with an interplanar spacing value of 0.59 nm, which corresponds to the strongest diffraction peak (2θ = 15.1°) in our measured XRD pattern. Therefore, the interplanar spacing of 0.59 nm originates from the (001) crystallographic plane of trigonal structured HfS$_2$. Further, similar interplanar spacing values of 0.57 nm and 0.58 nm were acquired for the recovered samples under non-hydrostatic and hydrostatic conditions, respectively. Meanwhile, the available well-resolved and periodic diffraction spots in the fast Fourier transform (FFT) patterns for the starting and recovered samples demonstrated that they exhibit high crystalline quality. Furthermore, all of these FFT patterns for HfS$_2$ can be identified as a trigonal crystalline system in the space group $P\bar{3}m1$. In short, the similar interplanar spacing values and FFT patterns for the starting and recovered samples proved the reversibility of the structural transitions under different hydrostatic environments.

Furthermore, the crystalline surface structure of the starting and recovered HfS$_2$ under different hydrostatic environments
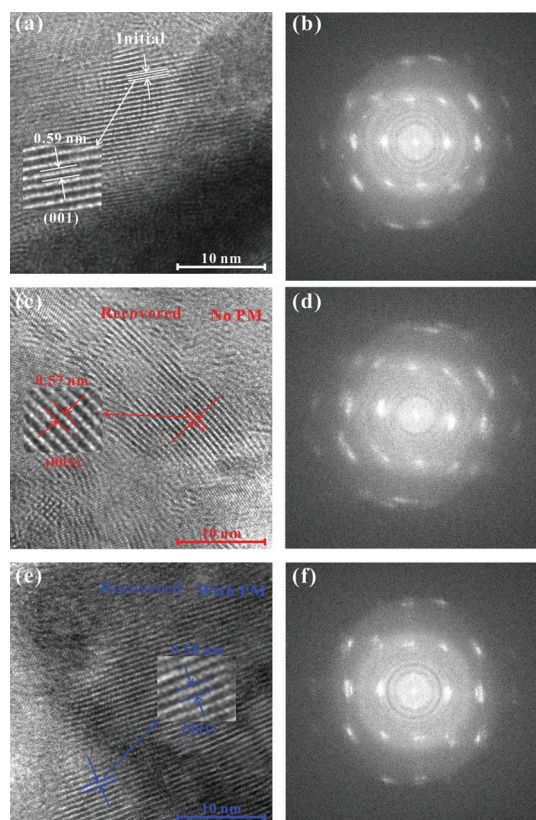

Fig. 6 HRTEM images and their corresponding FFT patterns for HfS$_2$. Herein, (a and b) are the starting sample; (c and d) represent the recovered sample decompressed from 38.2 GPa under non-hydrostatic conditions; (e and f) stand for the recovered sample released from 37.9 GPa pressure under hydrostatic conditions. The scale bar of the HRTEM image is 10 nm. Herein, PM indicates pressure medium.
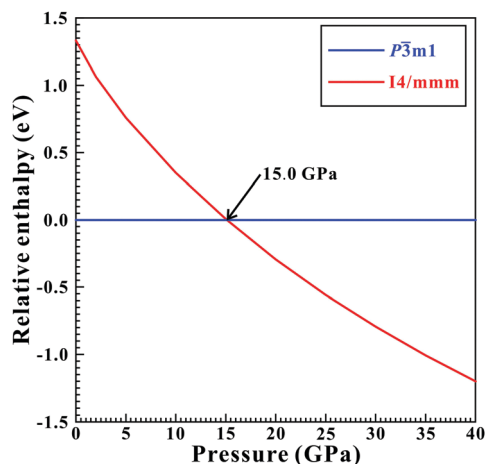
This journal is © The Royal Society of Chemistry 2022

J. Mater. Chem. C, 2022, **10**, 10541–10550 | **10547**

Paper

Fig. 7 The enthalpy difference between the $P\bar{3}m1$ and $I4/mmm$ phases in HfS$_2$ as a function of pressure at 0–40.0 GPa.

was checked by AFM observations, as shown in Fig. S4 (ESI†). From AFM results, the crystalline surface structures between the starting and recovered samples are similar, which also provides robust evidence for the reversibility of the pressure-induced structural transitions.

3.5 First-principles theoretical calculations results of HfS$_2$

To disclose the high-pressure structures of HfS$_2$, we calculated the enthalpies of the $P\bar{3}m1$ and $I4/mmm$ phases within the pressure range of 0–40.0 GPa. As shown in Fig. 7, the $P\bar{3}m1$ phase has a lower enthalpy compared with that of the $I4/mmm$ phase at 0–15.0 GPa, indicating the stability of the $P\bar{3}m1$ phase. As the pressure exceeded 15.0 GPa, the $I4/mmm$ phase was energetically more favourable than that of the $P\bar{3}m1$ phase. Therefore, our theoretical calculations results revealed the occurrence of a structural transition from the $P\bar{3}m1$ to $I4/mmm$ phases at 15.0 GPa, which is in good agreement with the second structural transition pressure of HfS$_2$ observed from the Raman scattering and electrical conductivity results under non-hydrostatic conditions. And thus, it makes sense that the first experimental observed phase transition of HfS$_2$ at $\sim$8.0 GPa is most possibly related to a second-order phase transition. As the pressure increased to $\sim$15.0 GPa, HfS$_2$ underwent a structural transition from the $P\bar{3}m1$ to $I4/mmm$ phase. Upon a further increase in the pressure to $\sim$20.0 GPa, the electrical conductivity results disclosed the occurrence of metallization in HfS$_2$, which was corroborated by the first-principles theoretical calculations results. Therefore, the third phase transition of HfS$_2$ was attributed to a metallization transition.

To further elaborate the underlying mechanism of metallization, first-principles theoretical calculations were implemented for HfS$_2$ at three representative pressures of 0, 10.0 and 20.0 GPa. Fig. 8 shows the calculated electronic band structures, density of states (DOS) and projected density of states (PDOS) along high-symmetry points in the Brillouin zone of HfS$_2$. Under ambient conditions, the calculated bandgap energy was 0.92 eV, which is smaller than the previous result with a bandgap energy of 1.23 eV.[34] Density functional theory (DFT)
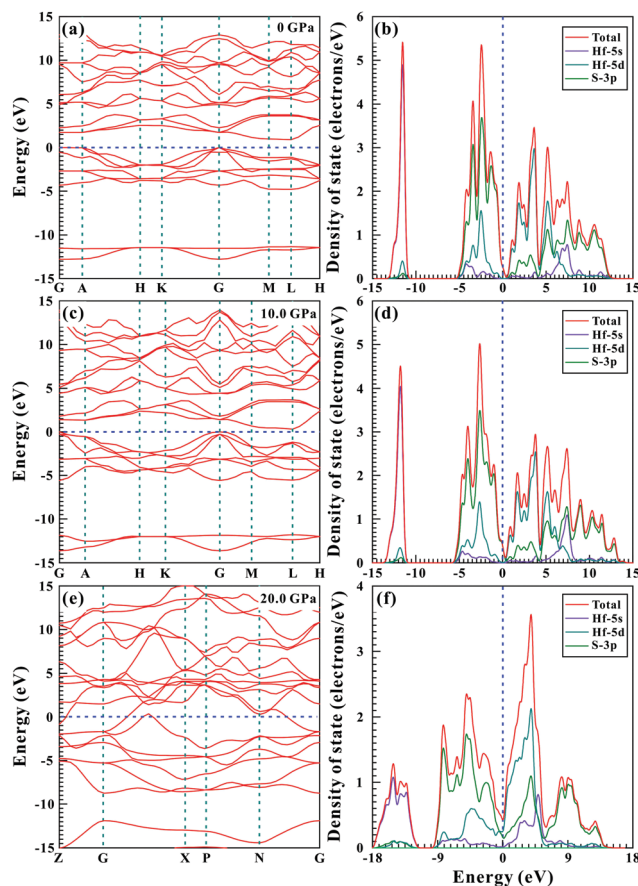

Fig. 8 (a, c and e) Calculated electronic band structures and (b, d and f) their correspondent density of states for HfS$_2$ at three representative pressures of 0, 10.0 and 20.0 GPa, respectively. Here, the Fermi level is displayed as a blue dotted line.

calculations generally underestimate the bandgap energy of TMDs, and thus, a slight discrepancy in bandgap energy is tolerated.[35] From Fig. 8b, the lowest valence bands between -15 eV and -10 eV primarily comprised the Hf-s state. Concurrently, the valence bands from -5 eV to 0 eV and the conduction bands were dominated by the Hf–d and S–p states. As depicted in Fig. 8c, the conduction bands widened more than the valence bands, resulting in an obvious decrease in the bandgap energy of HfS$_2$ with increasing pressure. Therefore, the bandgap energy of HfS$_2$ reduced substantially to 0.31 eV as the pressure was enhanced to 10.0 GPa. Upon further compression to 20.0 GPa, the overlap of the valence and conduction bands suggested the occurrence of metallization for HfS$_2$. Noteworthily, our predicted metallization pressure is in excellent agreement with the above-mentioned electrical conductivity results under non-hydrostatic conditions. Therefore, our observed metallization phenomenon for HfS$_2$ can be interpreted as the closure of the bandgap energy under high pressure.

Conclusions

We studied in detail the high-pressure structural and electronic characteristics of HfS$_2$ up to 42.1 GPa under different

hydrostatic conditions by means of multiple experimental methods of Raman spectroscopy, electrical conductivity, HRTEM and AFM coupled with first-principles theoretical calculations. Raman scattering and electrical conductivity results revealed that HfS_2 underwent two structural phase transitions at 8.0 GPa and 15.2 GPa, followed by a metallization at 20.5 GPa under non-hydrostatic conditions. However, higher structural phase transition and metallization pressures of 8.2, 17.2 and 23.1 GPa were observed for HfS_2 under hydrostatic conditions, which were ascribed to the influence of deviatoric stress. Our theoretical calculations results demonstrated that the closure in the bandgap energy was responsible for the metallization of HfS_2 under high pressure. Upon decompression, the reversibility of the structural transition was confirmed by our microscopic HRTEM and AFM results.

Author contributions

Lidong Dai and Haiying Hu conceived the idea and led the project. Meiling Hong, Xinyu Zhang and Chuang Li designed the experiments and performed the XRD, high-pressure Raman spectra, high-pressure electrical conductivity, HRTEM and AFM measurements. Meiling Hong and Yu He performed the first-principles theoretical calculations. Lidong Dai and Meiling Hong contributed to the analysis, interpretation and discussion of the results. Meiling Hong wrote the manuscript with the help of all the authors. All the authors commented on the final manuscript. Lidong Dai and Haiying Hu supervised the project.

Conflicts of interest

There are no conflicts to declare.

Acknowledgements

References

1 X. Zhao, C. Xia, T. Wang, X. Dai and L. Yang, *J. Alloys Compd.*, 2016, **689**, 302–306.
2 D. Singh and R. Ahuja, *ACS Appl. Energy Mater.*, 2019, **2**, 6891–6903.
3 N. Glebko, I. Aleksandrova, G. C. Tewari, T. S. Tripathi, M. Karppinen and A. J. Karttunen, *J. Phys. Chem. C*, 2018, **122**, 26835–26844.
4 D. Wang, X. Zhang, G. Guo, S. Gao, X. Li, J. Meng, Z. Yin, H. Liu, M. Gao, L. Cheng, J. You and R. Wang, *Adv. Mater.*, 2018, **30**, 1803285.
5 B. Zheng, Z. Wang, F. Qi, X. Wang, B. Yu, W. Zhang and Y. Chen, *Appl. Surf. Sci.*, 2018, **435**, 563–567.
6 M. Leem, H. Lee, T. Park, W. Ahn, H. Kim, E. Lee and H. Kim, *Appl. Surf. Sci.*, 2019, **509**, 144701.
7 Q. Zhao, Y. Guo, K. Si, Z. Ren, J. Bai and X. Xu, *Phys. Status Solidi B*, 2017, **254**, 1700033.
8 S. Mangelsen, P. G. Naumov, O. I. Barkalov, S. A. Medvedev, W. Schnelle, M. Bobnar, S. Mankovsky, S. Polesya, C. Näther, H. Ebert and W. Bensch, *Phys. Rev. B*, 2017, **96**, 205148.
9 H. N. Cruzado, J. S. C. Dizon, G. M. Macam, R. A. B. Villaos, T. M. D. Huynh, L. Feng, Z. Huang, C. Hsu, S. Huang, H. Lin and F. Chuang, *ACS Appl. Electron. Mater.*, 2021, **3**, 1071–1079.
10 Y. Xiao, M. Zhou, J. Liu, J. Xu and L. Fu, *Sci. China Mater.*, 2020, **38**, 753–760.
11 J. Ibáñez, T. Woźniak, F. Dybala, R. Oliva, S. Hernández and R. Kudrawiec, *Sci. Rep.*, 2018, **8**, 12757.
12 A. Andrada-Chacón, Á. Morales-García, M. A. Salvadó, P. Pertierra, R. Franco, G. Garbarino, M. Taravillo, J. A. Barreda-Argüeso, J. González, V. G. Baonza, J. M. Recio and J. Sánchez-Benítez, *Inorg. Chem.*, 2021, **60**, 1746–1754.
13 P. C. Klipstein, D. R. P. Guy, E. A. Marseglia, J. I. Meakin, R. H. Friend and A. D. Yoffe, *J. Phys. C: Solid State Phys.*, 1986, **19**, 4953–4963.
14 Y. Aoki, T. Sambongi, H. Takahashi, N. Mori, F. Levy and H. Berger, *Synth. Met.*, 1995, **71**, 1883–1884.
15 M. Grzeszczyk, J. Gawraczyński, T. Woźniak, J. Ibáñez, Z. Muhammad, W. Zhao, M. R. Molas and A. Babiński, *Acta Phys. Pol., A*, 2022, **141**, 95–98.
16 S. Klotz, J.-C. Chervin, P. Munsch and G. Le Marchand, *J. Phys. D: Appl. Phys.*, 2009, **42**, 075413.
17 K. Niwa, D. Nomichi, M. Hasegawa, T. Okada, T. Yagi and T. Kikegawa, *Inorg. Chem.*, 2011, **50**, 3281–3285.
18 M. Hong, L. Dai, H. Hu, X. Zhang, C. Li and Y. He, *Inorg. Chem.*, 2022, **61**, 4852–4864.
19 L. Dai, K. Liu, H. Li, L. Wu, H. Hu, Y. Zhuang, L. Yang, C. Pu and P. Liu, *Phys. Rev. B*, 2018, **97**, 024104.
20 D. Wang, X. Zhang and Z. Wang, *J. Nanosci. Nanotechnol.*, 2018, **18**, 7319–7334.
21 X. Zhang, L. Dai, H. Hu, M. Hong and C. Li, *RSC Adv.*, 2022, **12**, 2454–2461.
22 L. Yang, J. Jiang, L. Dai, H. Hu, M. Hong, X. Zhang, H. Li and P. Liu, *J. Mater. Chem. C*, 2021, **9**, 2912–2918.
23 S. J. Clark, M. D. Segall, C. J. Pickard, P. J. Hasnip, M. I. J. Probert, K. Refson and M. C. Payne, *Z. Kristallogr. - Cryst. Mater.*, 2005, **220**, 567–570.

24 Y. He, L. Dai, D. Y. Kim, H. Li and S.-I. Karato, *J. Geophys. Res.: Solid Earth*, 2021, **126**, e2021JB022939.

25 Y. He, S. Sun, D. Y. Kim, B. Jang, H. Li and H.-K. Mao, *Nature*, 2022, **602**, 258–262.

26 S. N. Neal, S. Li, T. Birol and J. L. Musfeldt, *npj 2D Mater. Appl.*, 2021, **5**, 45.

27 P. Saha, B. Ghosh, R. Jana and G. D. Mukherjee, *J. Appl. Phys.*, 2018, **123**, 204306.

28 X. Zhao, H. Liu, A. F. Goncharov, Z. Zhao, V. V. Struzhkin, H. K. Mao, A. G. Gavriliuk and X. Chen, *Phys. Rev. B*, 2019, **99**, 024111.

29 X. Wang, X. Chen, Y. Zhou, C. Park, C. An, Y. Zhou, R. Zhang, C. Gu, W. Yang and Z. Yang, *Sci. Rep.*, 2017, **7**, 46694.

30 Y. Zhuang, L. Dai, L. Wu, H. Li, H. Hu, K. Liu, L. Yang and C. Pu, *Appl. Phys. Lett.*, 2017, **110**, 122103.

31 Y. Zhuang, L. Dai, H. Li, H. Hu, K. Liu, L. Yang, C. Pu, M. Hong and P. Liu, *J. Phys. D: Appl. Phys.*, 2018, **51**, 165101.

32 D. Hou, Y. Ma, J. Du, J. Yan, C. Ji and H. Zhu, *J. Phys. Chem. Solids*, 2010, **71**, 1571–1575.

33 A. P. Nayak, S. Bhattacharyya, J. Zhu, J. Liu, X. Wu, T. Pandey, C. Jin, A. K. Singh, D. Akinwande and J. Lin, *Nat. Commun.*, 2014, **5**, 3731.

34 X. Yang, X. Qin, J. Luo, N. Abbas, J. Tang, Y. Li and K. Gu, *RSC Adv.*, 2020, **10**, 2615–2623.

35 J. Ruiz-Fuertes, S. López-Moreno, J. López-Solano, D. Errandonea, A. Segura, R. Lacomba-Perales, A. Muñoz, S. Radescu, P. Rodríguez-Hernández, M. Gospodinov, L. L. Nagornaya and C. Y. Tu, *Phys. Rev. B: Condens. Matter Mater. Phys.*, 2012, **86**, 125202.

10550 | *J. Mater. Chem. C*, 2022, **10**, 10541–10550

This journal is © The Royal Society of Chemistry 2022